Experimental characterization and numerical modeling of the influence of a proof load on the fatigue resistance of welded structures

H. Heyraud [a,*], C. Mareau [a], F. Lefebvre [b], P. Amuzuga [b], R. Hauteville [b], F. Morel [a], L. Jubin [b], D. Bellett [a], T. Leblanc [b]

[a] Arts et Metiers Institute of Technology, LAMPA, HESAM Université, F-49035 Angers, France
[b] CETIM, 52 Av. Félix Louat, 60300, Senlis, France

Keywords:
Fatigue resistance
Welded structures
Loading ratio
Residual stresses
Strain hardening

A B S T R A C T

The influence of a proof load, or an initial overload, on the fatigue resistance of welded structures is investigated in this study. Arc welded stiffeners made of S355 steel are considered and fatigue-tested in as-welded and proof-loaded conditions. X-ray diffraction analyses are carried out to evaluate the influence of a proof load on the residual stress field. To better understand the role of a proof load on the mechanical fields in the stress concentration zones, a numerical approach based on elasto-plastic finite element analyses is proposed. The methodology includes a non-local multiaxial fatigue criterion, which integrates a strain hardening contribution, that makes it possible to estimate the number of cycles to failure. The comparison between experimental and numerical results indicates that the beneficial effect of a proof load on the fatigue resistance can be mainly attributed to residual stress and strain hardening effects. The final result is a master SN curve adapted to the fatigue design of stiffener structures, tested under different loading conditions.

1. Introduction

Welding is one of the most common process for the assembly of metallic structural components. To assess the integrity of welded structures, a proof load is sometimes applied before service, and it is even imposed by certain standards [1]. It consists of applying an initial overload to the structure to ensure the structural integrity of mechanical systems. This is usually carried out after manufacture but before the equipment is put into service, and typically without regard to the consequences in terms of fatigue life in service. To evaluate the impact of a proof load on the fatigue resistance of welded steel structures, different experimental studies have been conducted. For instance, Masumoto et al. [2] applied a strain-controlled preload, in tension to butt-welded specimens. These specimens were then fatigue-tested under tensile cyclic loads, with a positive load ratio. According to the results, the application of a nominal tensile strain of 4% leads to an increase in the fatigue resistance of 20% in comparison with as-welded specimens. The authors attribute the beneficial effect of the preload to the presence of compressive residual stresses at the weld toe. Hensel et al. [3] studied the consequences of a proof load on the residual stress field of arc-welded longitudinal stiffeners made out of S355 steel. The residual stress state in as-welded and proof-loaded conditions (98% of the yield strength) was evaluated. In the critical zone, the proof load eliminated the tensile residual stresses induced by welding. Fatigue tests under reverse tension were also conducted. In comparison with as-welded structures, an increase of the fatigue resistance of 240% was observed for proof-loaded structures. Sadeler et al. [4] evaluated the effect of compressive residual stresses induced by a preload on the fatigue life of notched specimens (notch radius of 2 mm, $K_t = 1.84$) made of AISI 4140 steel. In comparison with as-welded specimens, an improvement of about 36% in fatigue life of prestrained specimens was observed.

Since conventional experimental techniques (e.g. X-ray diffraction, hole drilling) do not provide full insight into the residual stress re-distribution resulting from the application of a proof load, numerical simulation has been used as an alternative investigation method. Tsutsumi et al. [5] evaluated the beneficial effect of a proof load on the fatigue resistance of U-rib steel welded specimens. For this purpose, a 2D elasto-plastic finite element model was developed. A fatigue criterion, which integrates the influence of residual stresses, was then proposed. According to the authors, the compressive residual stresses resulting from a proof load must be considered to obtain numerical results consistent with experimental observations. Schubnell et al. [6] considered transverse stiffeners made of mild S355J2 steel and evaluated the consequences of a HFMI-treatment followed by a single overload on the residual stress field. For this purpose an elasto-plastic

* Corresponding author.
E-mail address: hugo.heyraud@ensam.eu (H. Heyraud).

https://doi.org/10.1016/j.ijfatigue.2023.107604

List of Symbols

α	Maximal hydrostatic pressure sensitivity coefficient
$\dot{p}$	Plastic multiplier
λ, μ	Lamé coefficients
$\overline{\sigma_{eq}}$	Equivalent stress
$\overline{\sigma_{VM}}$	Volume average of the von Mises stress
$\overline{\sqrt{J2}_a}$	Volume average of the octahedral shear stress amplitude
$\overline{P_m}$	Volume average of the maximum hydrostatic pressure
ϕ	Strain hardening sensitivity exponent
ρ	Radius of the integration sphere
Σ	Stress tensor
σ_{nom}	Nominal stress
Σ_{rs}	Residual stress tensor
σ_{VM}	Von Mises stress
σ_{y0}	Initial yield stress
$\sqrt{J2}_a$	Octahedral shear stress amplitude
C_k, γ	Material parameters
E	Strain tensor
F	Load
I	Identity tensor
m, C	Basquin parameters
N	Number of cycles to failure
P_m	Maximum hydrostatic pressure
P_{rs}	Residual hydrostatic pressure
R	Loading ratio
S_0	Nominal section
t	Time
U_ψ	Displacement in the ψ direction
V	Volume of the averaging sphere
X	Backstress tensor

finite element model was developed considering different material behavior for the base metal, the heat affected zone and the welded area. The residual stress numerically predicted were then compared to experimental analysis. According to the authors, the HFMI-treatment and the single tensile overload affect the residual stresses field and consequently influence the fatigue strength. While the beneficial effect of a proof load is mostly attributed to the modification of the residual stress field in critical zones [7,8], Masumoto et al. [2], Schubnell et al. [6,8], Leitner et al. [9] and Janardhan et al. [10] also mentioned the role of strain hardening. Indeed, while different studies have concluded that there is a beneficial effect of strain hardening on the fatigue resistance of homogeneous specimens [11–13], the role of strain hardening on the fatigue resistance of welded structures remains unclear. Also, in the aforementioned studies, no attention has been given to the influence of the load ratio on the fatigue resistance of proof-loaded structures.

In the present study, the impact of a proof load on the fatigue resistance of as-welded steel structures is investigated. For this purpose, experimental fatigue tests on stiffener structures were performed. Two load ratios are considered and the impact of the mean load on the fatigue resistance of as-welded and proof-loaded structures is also evaluated. In addition, to further analyze the experimental results, numerical simulations based on the finite element method were conducted. Specifically, an elasto-plastic model is used to evaluate the stress field resulting from the application of a proof load and a cyclic load. The stress field is finally post-processed with a non-local fatigue Crossland criterion. This criterion is a modified version of that initially proposed by El May et al. [14] for corrosion defects. Specifically, an additional contribution of stress history effects is included in the non-local criterion to describe the impact of a proof load on the fatigue resistance of welded structures. Such a criterion makes it possible to discuss the impact of the proof load and the load ratio on the residual stress field and local strain hardening. It also allows for the construction of a single master curve adapted to the fatigue design of welded stiffeners with different loading conditions.

This article is divided into four sections with both experimental and numerical aspects. The specimen geometry and the different experimental methods are detailed in the first section. The numerical approach and the fatigue criterion are described in the second section. The experimental and numerical results are presented in the third section and confronted and discussed in the last section.

2. Experimental methods

2.1. Specimen geometry

The present study focuses on the fatigue resistance of welded stiffeners, which were made of 8 mm thick S355 structural steel sheets. The corresponding geometry is shown in Fig. 1. For the fabrication of the stiffeners, the different plates were first positioned with respect to each other and spot welded. It is worth mentioning that the spot welds were positioned away from the critical zones for fatigue failure. A robotic Metal Active Gas (MAG) welding process was then used with a copper-coated solid wire and an argon/CO2/O2 gas to construct the weld seams with a single welding pass. The weld starts and weld ends were positioned away from the critical zones of fatigue failure (see Fig. 2). Also, it is worth mentioning that only nominal weld dimensions were used for the present study, i.e., the real geometry of the weld seam was not considered.

2.2. Specimen characterization

2.2.1. Hardness measurements

To evaluate the mechanical property gradients, Vickers hardness measurements were conducted according to the EN ISO 9015-2 standard. For each characteristic zone of the welded structures (base metal, heat-affected zone and fusion zone), at least 6 hardness measurements were carried out with a load of 200 g and a dwell time of 10 s.

2.2.2. Residual stress analysis

In the present study, X-ray Diffraction (XRD) techniques were used to evaluate the impact of a proof load on the residual stress state at the surface of a stiffener structure. XRD analyses were performed according to the EN 15305-2009 standard using an X-RAYBOT V2 apparatus equipped with a chromium anode. As shown in Fig. 2, the analyzed zone, which is circular (with a diameter of 2 mm), is adjacent to the weld toe. Prior to XRD analyses, the area of interest was electropolished to a depth of 100 µm. XRD stress analyses were then conducted in-situ for successive proof loads with increasing intensity (from 0 to 420 MPa nominal stress calculated in the longitudinal plate). After each proof load, the residual stress state $\mathbf{\Sigma_{rs}}$ was estimated from the 2θ position of {211} lattice planes by assuming a biaxial stress state. The residual hydrostatic pressure P_{rs} was deduced from $\mathbf{\Sigma_{rs}}$ according to:

$$P_{rs} = \frac{1}{3}\mathrm{tr}(\mathbf{\Sigma_{rs}}). \quad (1)$$

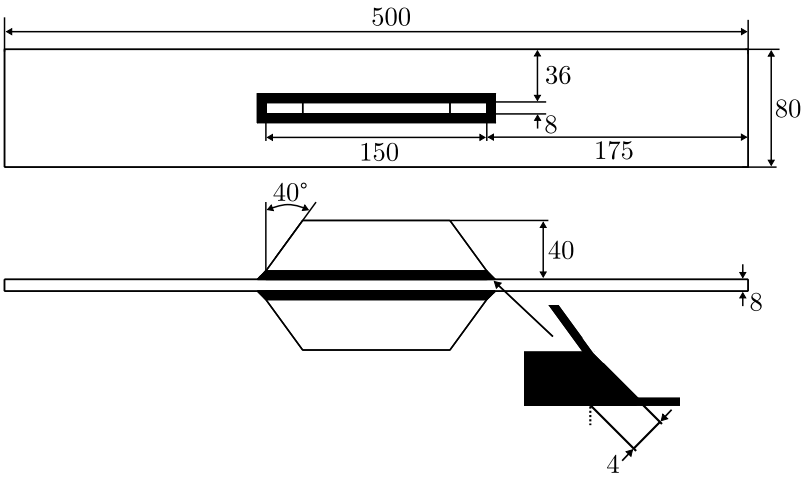

Fig. 1. Dimensions (in millimeters) of the investigated stiffener structures.

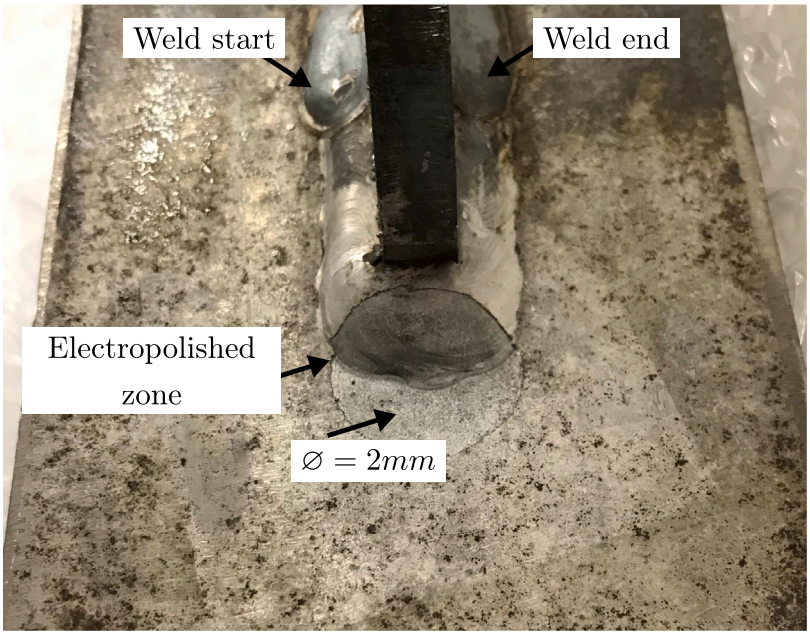

Fig. 2. Position of the electropolished zone and the spot in which the residual stress analysis was done.

2.2.3. Fatigue tests

The fatigue resistance of the stiffener structures was evaluated via a vast experimental campaign using a uniaxial tension-compression servo-hydraulic machine. The specimens were clamped on 50 mm at both extremity of the flange as shown in Fig. 3. The tests were carried out under load control with a frequency of 10 Hz and a load ratio R of either 0.1 or −1 until the total fracture occurred. A number of cycles of 10^7 was used as the runout condition. Prior to fatigue testing, some of the specimens were proof-loaded with either tensile or compressive loads. Due to possible geometrical distortion induced by the welding process, an anti-buckling fixture [15] was used to apply the compressive proof-load in order to limit as possible secondary bending in the specimens. For the definition of the different loading conditions, the nominal stress σ_{nom} is used:

$$\sigma_{nom} = \frac{F}{S_0} \tag{2}$$

where F is the prescribed load and S_0 the nominal section of the axial plate of the specimen. The loading conditions used for the present study are summarized in Table 1.

3. Numerical methods

To evaluate the impact of a proof load on the fatigue resistance of welded structures, a non-local fatigue criterion is proposed. This criterion relies on the elasto-plastic finite element method (FEM) to compute the stress field resulting from the loading history (i.e., the proof load followed by the cyclic loads). The main features of the FEM model are presented in the next section.The Abaqus solver was used for the application of the finite element method. The constitutive equations used to represent the elasto-plastic behavior of the structural steel are then detailed. The non-local fatigue criterion that is used to post-process the FEM simulations is finally described.

3.1. Geometry, mesh generation and boundary conditions

To evaluate the stress field resulting from a loading sequence, a finite element model of the stiffener structure has been constructed. As shown in Fig. 4, this model uses an idealized representation of the weld toe with no fillet radius. Also, the nominal dimensions of welded structures were used to construct the finite element model. As a result,

Table 1
Summary of the experimental fatigue campaign — Loading conditions investigated to establish the fatigue resistance of stiffener structures.

Proof load nominal pre-stress (MPa)	Fatigue applied nominal stress range (MPa)							R	Number of specimens			
0	77	113		169			253	0.1	4	4	4	4
281			140	169	197	225		0.1	5	4	4	4
352			140		197		253	0.1	4	5		4
375				169				0.1			5	
422							253	0.1			4	
−352		113						0.1			3	
0				169			253	−1		4		4
352				169			253	−1		4		4
−352				169			253	−1		2		4

Fig. 3. Stiffener structure clamped on the servo-hydraulic machine.

dimensional errors, such as the perpendicularity defect between the stiffeners and the base plates or the non-flatness of the base plates, were not considered. For the application of the finite element method, the structure was meshed with second order tetrahedral elements. An isotropic mesh size of 50 μm was assigned to the elements located in a cylinder with a 0.5 mm radius around the weld toe. The mesh size was gradually increased to 2 mm toward the global structure as shown in Fig. 4. The Fig. 5 gives the results of a preliminary mesh convergence study and show that a mesh size of 50 μm is sufficient to limit mesh dependency. Specifically, while the local stress state may depend on the mesh size because of stress singularities, the averaging procedure presented hereafter allows computing volume-averaged stress quantities whose dependence with respect to mesh resolution is negligible. The boundary conditions are also show in Fig. 4. The axial load F is represented as an evenly distributed pressure applied on one of the specimen end. The axial displacement is blocked on the opposite end. Additional Dirichlet boundary conditions are also included to prevent rigid body motions.

3.2. Constitutive model

To consider the accumulation of plastic strains resulting from a loading sequence, an elasto-plastic constitutive model is used. In the context of infinitesimal transformations, the total strain tensor $\boldsymbol{E}$ is additively decomposed into elastic $\boldsymbol{E}^e$ and plastic $\boldsymbol{E}^p$ contributions:

$$\boldsymbol{E} = \boldsymbol{E}^e + \boldsymbol{E}^p. \tag{3}$$

For isotropic materials, the stress tensor $\boldsymbol{\Sigma}$ is obtained from the elastic strain tensor $\boldsymbol{E}^e$ with:

$$\boldsymbol{\Sigma} = \lambda \mathrm{tr}(\boldsymbol{E}^e)\boldsymbol{I} + 2\mu \boldsymbol{E}^e. \tag{4}$$

where λ and μ are the Lamé coefficients. To determine whether the conditions for plastic flow are met or not, the von Mises yield criterion is adopted. For this purpose, it is convenient to introduce the von Mises equivalent stress σ_{VM} such that[1]:

$$\sigma_{VM} = \sqrt{\frac{3}{2}(\boldsymbol{\Sigma}^d - \boldsymbol{X}^d) : (\boldsymbol{\Sigma}^d - \boldsymbol{X}^d)}, \tag{5}$$

where $\boldsymbol{X}$ is the backstress tensor resulting from kinematic hardening. According to the experimental results of Gadouini et al. [17], Slezak and Sniezek [18] and Giraud [19], who characterized of the cyclic behavior of a S355 steel, the size of the elastic domain is not significatively affected by the plastic deformation. As a result, a reasonable description of the cyclic behavior is obtained when a pure kinematic description of the hardening is adopted. The corresponding yield function f is thus given by:

$$f = \sigma_{VM} - \sigma_{y0}, \tag{6}$$

where σ_{y0} is the initial yield stress. The kinematic hardening rule of Frederick and Armstrong [20] is used to describe the cyclic behavior of the different regions of the structure. According to the results of Gadouini et al. [17], this non-linear hardening rule provides a reasonable description of the cyclic behavior of the S355 steel grade. The expression of the hardening rule is:

$$\dot{\boldsymbol{X}} = \frac{C_k}{\sigma_{y0}}(\boldsymbol{\Sigma} - \boldsymbol{X})\dot{p} - \gamma \boldsymbol{X}\dot{p}. \tag{7}$$

In the above equation, $\dot{p}$ is the plastic multiplier and C_k and γ are two material parameters controlling the initial hardening rate and the asymptotic value of the backstress tensor. The material characterization of the heat affected zone and the welded metal were not considered in this study, therefore a more sophisticated hardening model was not envisaged. The microstructure of the weld metal, which is largely controlled by the local thermal history, is assumed to be heterogeneous. Depending on the local microstructure, a seam weld is conventionally divided into three regions: the base metal, the heat-affected zone and the fusion zone. To model the elasto-plastic behavior of the weld metal, two different descriptions are tested in the following. The first strategy, which is referred to as the heterogeneous description, considers different sets of material parameters for the different zones. The geometry of the three zones considered in the models are shown in Fig. 6. The second strategy, which is referred to as the homogeneous description, ignores microstructural gradients, hence uses a single set of material parameters for the whole structure.

3.3. Fatigue criterion

To evaluate the fatigue resistance of welded structures tested with different loading conditions, a non-local multiaxial fatigue criterion is proposed [21–23]. Such a criterion relies on the definition of an equivalent stress $\overline{\sigma}_{eq}$ to evaluate the number of cycles to failure N for a given loading history. According to this approach, fatigue crack

[1] The superscript d denotes the deviatoric part of a second rank tensor.

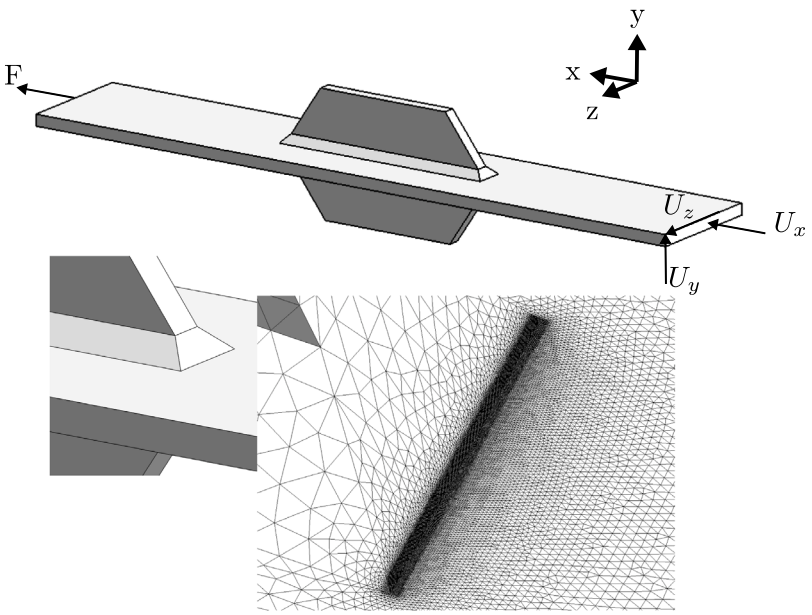

Fig. 4. Boundary conditions used in the finite element model and mesh refinement in the critical zone, element size 50 μm.

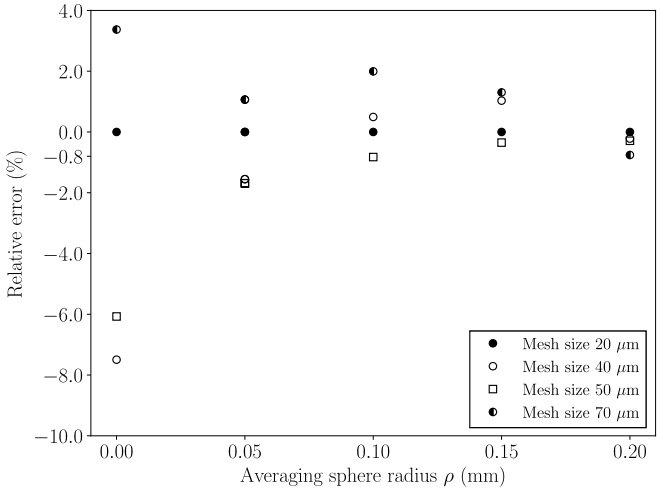

Fig. 5. Mesh convergence study based on the equivalent stress presented at the Section 3.3 and considering the mesh size of 20 μm as the reference one [16].

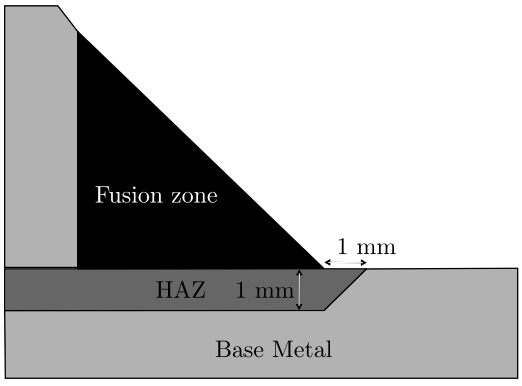

Fig. 6. Geometry of the heat affected zone (HAZ) considered in the model.

initiation after N loading cycles occurs when the maximum value of the equivalent stress equals the fatigue resistance:

$$\max_{\boldsymbol{x}}(\overline{\sigma}_{eq}(\boldsymbol{x})) = \beta(N), \tag{8}$$

where $\beta(N)$ is the fatigue resistance corresponding to a given number of cycles to failure N. In the present work, the Basquin equation [24] is used to include the number of cycles to failure in the expression of the fatigue resistance:

$$\beta = \frac{C}{N^m}, \tag{9}$$

where m and C are the Basquin parameters. According to Eq. (8), the number of cycles to failure N is therefore given by:

$$N = \frac{C}{\max_{\boldsymbol{x}}(\overline{\sigma}_{eq}(\boldsymbol{x}))^m}. \tag{10}$$

The evaluation of the equivalent stress $\overline{\sigma}_{eq}$ is based on the Crossland criterion [25]. According to the literature, this criterion, which was selected here mostly for simplicity reasons, provides a reasonable description of the impact of stress multiaxiality on the fatigue resistance of welded structures [26,27]. In contrast with the original proposition of Crossland [25], the equivalent stress is non-local in the sense that it is obtained from a spatial averaging procedure. The non-locality is introduced to (i) limit the FE mesh dependency and (ii) to take into account the stress gradients that affect the fatigue resistance [28–30]. The non-local equivalent stress is computed from the volume average of the octahedral shear stress amplitude $\overline{\sqrt{J2}_a}$ and the volume average of the maximum hydrostatic pressure $\overline{P}_m$. As shown in Fig. 7, these quantities are obtained from their local counterparts $\sqrt{J2_a}$ and P_m with a volume averaging operation applied in a sphere with radius ρ according to:

$$\overline{\sqrt{J2}_a}(\boldsymbol{x}) = \frac{1}{V(\boldsymbol{x})}\int_V \sqrt{J2}_a(\boldsymbol{x}')\, d\boldsymbol{x}', \tag{11}$$

$$\overline{P}_m(\boldsymbol{x}) = \frac{1}{V(\boldsymbol{x})}\int_V P_m(\boldsymbol{x}')\, d\boldsymbol{x}', \tag{12}$$

where V denotes the volume of the averaging sphere.

Different studies have shown that the fatigue resistance of metallic materials is affected by strain hardening [2,11,31,32]. To consider the influence of strain hardening, the present study assumes that the fatigue resistance increases when the maximum von Mises stress obtained during a loading history exceeds the initial yield stress. It is therefore

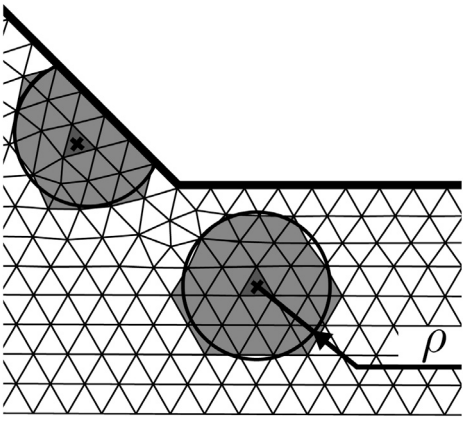

Fig. 7. 2D representation of the integration sphere. The parameter ρ defines the radius of the integration sphere for the computation of the non-local fatigue criterion.

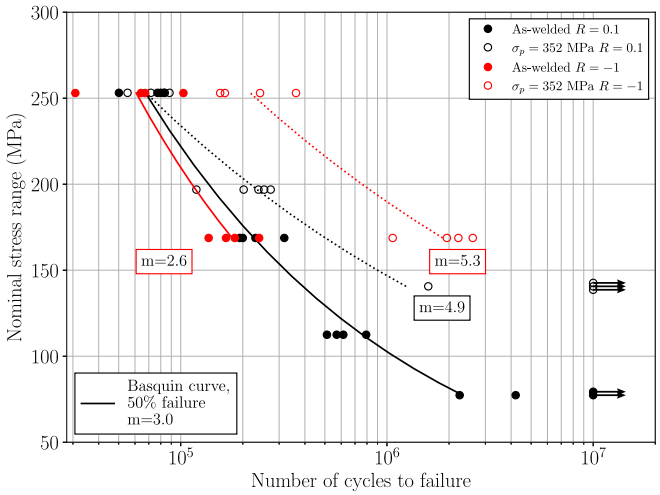

Fig. 8. S–N curves obtained for as-welded and proof-loaded stiffener structures for different load ratios. An initial nominal stress of 352 MPa was applied before cyclic loading for the proof-loaded stiffener structures.

convenient to introduce a hardening factor h (with $0 < h \leq 1$) for any material point such that:

$$h(\boldsymbol{x}) = \left(\frac{\sigma_{y0}(\boldsymbol{x})}{\max_t(\sigma_{y0}(\boldsymbol{x}), \overline{\sigma}_{VM}(\boldsymbol{x}, t))} \right)^{\phi}, \tag{13}$$

where t is the time, ϕ is a material parameter that controls the contribution of the strain hardening and $\overline{\sigma}_{VM}$ is the average von Mises stress:

$$\overline{\sigma}_{VM}(\boldsymbol{x}, t) = \frac{1}{V(\boldsymbol{x})} \int_V \sigma_{VM}(\boldsymbol{x}', t)\, d\boldsymbol{x}'. \tag{14}$$

The hardening factor h is constructed in such a way that it takes a unit value if the initial yield stress is not exceeded during a loading history. Alternatively, when plastic yielding occurs, the hardening factor is reduced. Such a strategy allows considering that the impact of an initial plastic straining (i.e., overload) on the fatigue resistance strongly depends on the difference between the maximum stress obtained during the initial loading and that obtained during cyclic loading. Specifically, when an initial plastic strain is applied, the maximum von Mises stress obtained during the initial loading is superior to the initial yield stress. The h factor is thus inferior to unity, which reduces the severity of the cyclic loading measured by the Crossland equivalent stress.

$$\overline{\sigma}_{eq}(\boldsymbol{x}) = \left(\overline{\sqrt{J2}}_a(\boldsymbol{x}) + \alpha \overline{P}_m(\boldsymbol{x}) \right) \cdot h(\boldsymbol{x}), \tag{15}$$

$$= \left(\overline{\sqrt{J2}}_a(\boldsymbol{x}) + \alpha \overline{P}_m(\boldsymbol{x}) \right) \cdot \left(\frac{\sigma_{y0}(\boldsymbol{x})}{\max_t(\sigma_{y0}(\boldsymbol{x}), \overline{\sigma}_{VM}(\boldsymbol{x}, t))} \right)^{\phi}. \tag{16}$$

The evaluation of the non-local Crossland equivalent stress uses three material parameters: ρ the averaging sphere radius to account for the effects of stress gradients, α the maximal hydrostatic pressure sensitivity coefficient and ϕ the strain hardening sensitivity exponent. The original form of the Crossland criterion [25] is obtained when both ρ and ϕ are zero.

4. Results

4.1. S-N curves for stiffener structures

4.1.1. Influence of the loading ratio

The experimental S–N curves, showing the nominal stress range as a function of the number of cycles to failure for the stiffener structures, are shown in Fig. 8 and a summary of the fatigue test results is given in Table 4. The Basquin curve parameters were identified by linear regression taking stress amplitude as the independent variable and plotted [24]. The results obtained for loading ratios of −1 and 0.1 are presented for as-welded and proof-loaded specimens. For proof-loaded specimens, an initial nominal stress of 352 MPa was applied before cyclic loading. According to these results, the load ratio has no significant influence on the fatigue resistance for as-welded specimens. Such results are consistent with those obtained by Baumgartner and Bruder [33] and Hensel et al. [3] on similar structures. Alternatively, proof-loaded structures tested with a load ratio of −1 display a higher fatigue resistance than those tested with a load ratio of 0.1. The application of a proof load therefore affects the mean load sensitivity of the structure.

4.1.2. Influence of the proof load intensity

The nominal S–N curves obtained for proof-loaded stiffener structures with load ratios of 0.1 and −1 are presented in Fig. 9. Different proof loads were applied before cyclic loading. The investigated proof load values, corresponding to nominal axial stress, were varied between −352 MPa and 422 MPa. The results obtained for as-welded specimens are also included. It can be seen from Fig. 9 that a beneficial effect on the fatigue resistance is observed when the proof load exceeds 250 MPa. For moderate or negative proof loads (≤ 250 MPa), no beneficial, nor detrimental effect is detected. Also, the beneficial effect of a proof load is more visible for low nominal stress ranges. Such results indicate that the difference between the maximum nominal stress applied during the proof load and the maximum nominal stress of the cyclic loading controls the impact of the proof load.

4.2. Material parameters

4.2.1. Constitutive model parameters

For the application of the elasto-plastic constitutive model, the Lamé coefficients (λ and μ) were taken as being identical for the different zones. They correspond to a Young's modulus of 210 GPa and a Poisson's ratio of 0.3. When the heterogeneous description of the stiffener structure is adopted, a set of hardening parameters must be assigned to each of the three regions (base metal, heat-affected zone and fusion zone). In the present study, it was not possible to evaluate the local mechanical behavior and to determine the material parameters corresponding to the different zones. Indeed, the heat-affected zone extends only up to 1 mm from the weld toe, which makes it difficult to extract representative specimens from each zone. To circumvent this difficulty, the empirical relations proposed by Hart [34] are used. Specifically, Hart [34] established empirical relationships

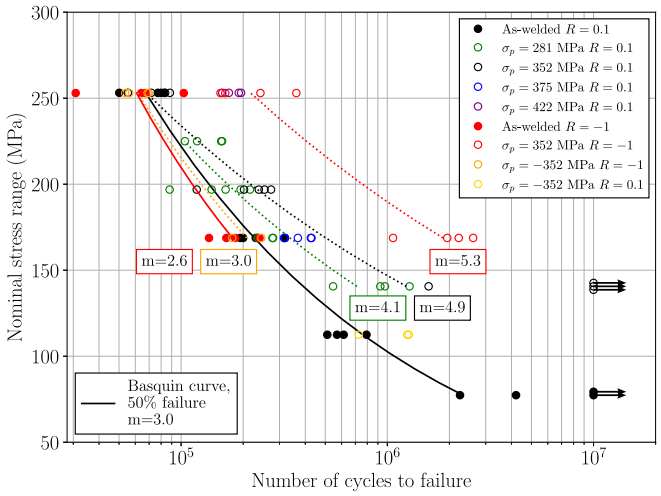

Fig. 9. S–N curves obtained for as-welded and proof-loaded stiffener structures for different load ratios. Nominal proof loads from −352 MPa to 422 MPa were applied before cyclic loading.

Table 2
Parameters of the constitutive equations used to model the material behavior of the base metal, the heat-affected zone and the fusion zone.

Zone	Hardness (HV)	σ_{y0} (MPa)	C_k (MPa)	γ
Base metal	185	350	7700	30.4
Heat affected zone	225	382	10 550	30.4
Fusion zone	205	545	3500	30.4

between the Vickers hardness and the yield stress for the base metal, the heat-affected zone and the fusion zone of welded steels. These relationships make it possible to determine the initial yield strength σ_{y0} for the different zones. Also, the kinematic hardening parameters C_k and γ were obtained from the results of Hiraide et al. [35], who performed strain-controlled cyclic tests on specimens with different hardnesses, for a similar steel grade. The material parameters obtained for the different zones are given in Table 2 with the corresponding Vickers hardness. These parameters were used for both the initial and cyclic loading. For the purpose of illustration, the stress–strain curves obtained for the different zones for a uniaxial Bauschinger test (tension then compression) are displayed in Fig. 10.

For the homogeneous description, the hardening parameters associated with the heat-affected zone are used for the entire structure. As discussed hereafter, the critical region for fatigue crack initiation is located within the heat-affected zone. In the other regions (base metal and fusion zone), plastic deformation is usually limited and an accurate estimation of the hardening parameters is not essential for the evaluation of the overall behavior of the stiffener structure.

4.2.2. Fatigue criterion parameters

The non-local fatigue criterion includes five different material parameters: the radius of the integration sphere ρ, the maximum hydrostatic pressure sensitivity coefficient α and the strain hardening sensitivity exponent ϕ and the Basquin parameters C and m. It is worth mentioning that the radius of the integration controls the sensitivity of the fatigue criterion to stress gradients. The effect of the mean stress state, which includes the residual stress state, is controlled with the maximum hydrostatic pressure sensitivity coefficient. Finally, as discussed earlier, the impact of strain hardening on the fatigue resistance can be adjusted with the ϕ exponent. For the identification of these parameters, an optimization procedure has been used. Such a procedure aims at finding the set of parameters that maximize the linear correlation coefficient between the observed and calculated number of cycles to failure. This procedure has been applied for both the homogeneous and heterogeneous descriptions of the stiffener structure. The corresponding sets of parameters are presented in Table 3.

Table 3
Set of parameters identified for the homogeneous and heterogeneous behaviors and the corresponding range of parameters and increments that were investigated.

Parameters	Heterogeneous	Homogeneous	Range, increment
ρ mm	0.1	0.1	[0.05–0.5], 0.05
α	0.2	0.3	[0–0.4], 0.1
ϕ	0.4	0.4	[0–0.5], 0.1
m N/MPa	4.5	4.6	[2–6], 0.1
log_{10} C N MPa	15.7	16,2	[10–20], 0.05

The experimental and numerical number of cycles to failure obtained for the different loading conditions are compared to each other in Figs. 11 and 12. The Pearson correlation coefficient r^2, which quantifies the correlation between numerical and experimental data, is also calculated. For both descriptions (homogeneous $r^2 = 0.82$ or heterogeneous $r^2 = 0.84$), only minor differences are observed between the numerical and experimental data for structures tested with a loading ratio of $R = 0.1$. Such results indicate that an accurate estimate of material properties is not of prime importance for the evaluation of the fatigue resistance of as-welded and proof-loaded structures. For the application of the fatigue criterion, the residual stresses from welding were not considered. For all the tested configurations, the yield stress within critical zones is exceed. The accumulation of plastic strains is therefore expected to eliminate the residual stresses resulting from welding operations. The sole exception to this situation is the case of structures that were not proof-loaded and tested with a loading ratio $R = -1$. For this specific case, the fatigue behavior may be influenced by welding-induced residual stresses. This aspect is discussed in Section 5.3

4.3. Influence of a proof load on the residual stress state

Fig. 13 shows the residual hydrostatic pressure, obtained both experimentally and numerically, at the weld toe immediately after a proof load, plotted as a function of the nominal proof stress. In terms of the experimentally determined values, the residual hydrostatic pressure is positive (about 180 MPa) for the as-welded state, which indicates that significant tensile residual stresses are present. When an initial proof load is applied, the residual hydrostatic pressure is progressively shifted toward negative values. Such results are consistent with those obtained by Wang et al. [36] for an aluminum alloy and by Farajian et al. [7] for a S690QL steel grade. For severe proof loads, the residual hydrostatic pressure saturates to a lower limit of approximately −70 MPa. It is worth mentioning that the saturation of the residual hydrostatic pressure occurs when the nominal proof stress exceeds the yield stress of the base material (≈ 350 MPa), which corresponds to the macroscopic plastification of the structure.

The results obtained with the numerical models, for both descriptions (i.e., homogeneous and heterogeneous) are also included in Fig. 13. When the initial residual stresses are not considered, the model predictions are consistent with the experimental observations for significant proof loads (≥ 220 MPa). Also, even though the homogeneous description provides slightly better results, both descriptions lead to similar results with a minimum residual hydrostatic pressure of approximately −70 MPa. To evaluate the impact of an initial residual stress field on the redistribution of the residual stress field, additional simulations were conducted with an initial residual hydrostatic pressure of 230 MPa, using the homogeneous description of the structure. The results show that except for the initial state, the difference between the model previsions obtained with and without an initial residual stress field is less than 20 MPa for the smallest proof load. This indicates that the initial residual stress field does not need to be considered for the evaluation of proof load-induced residual stresses, provided that the nominal proof stress is superior to 220 MPa.

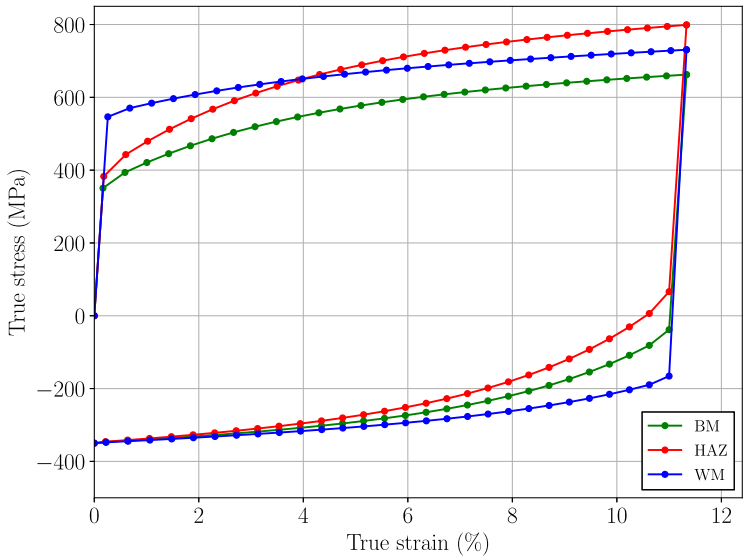

Fig. 10. Stress–strain curves calculated with the elasto-plastic model for a uniaxial Bauschinger test (tension then compression) for the different zones: base metal (BM), heat-affected zone (HAZ), fusion zone (FZ).

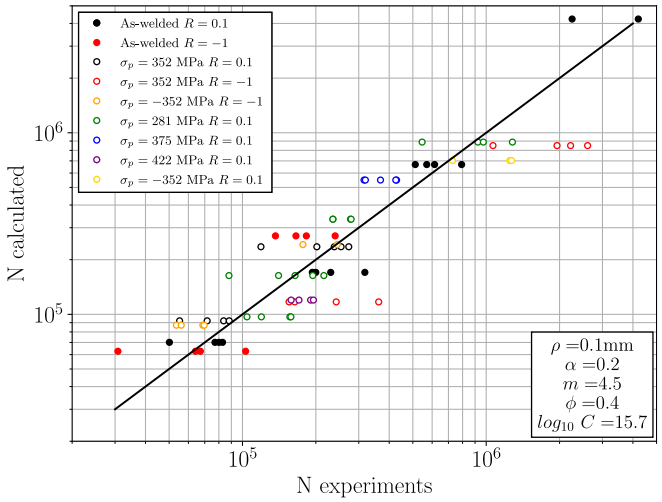

Fig. 11. Number of cycles to failure calculated with the numerical model using the heterogeneous description, as a function of the experimental number of cycles to failure.

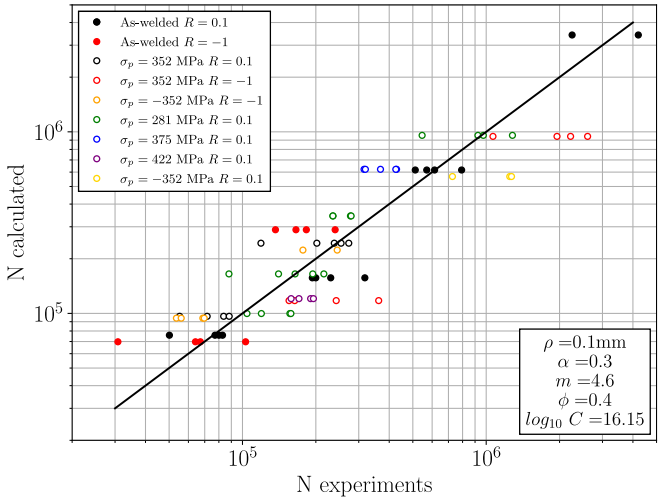

Fig. 12. Number of cycles to failure calculated with the numerical model, using the homogeneous description, as a function of the experimental number of cycles to failure.

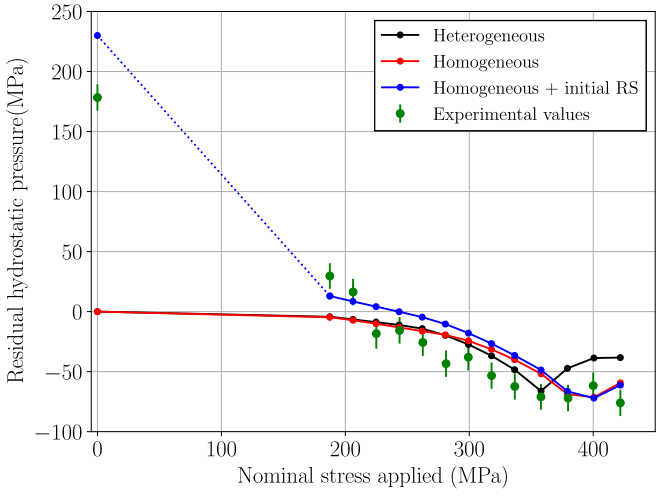

Fig. 13. Comparison between the residual hydrostatic pressure determined experimentally and via numerical simulations after proof load. The dotted line indicates a region where interpolation between the corresponding data points is uncertain.

5. Discussion

5.1. Role of microstructural gradients

The numerical models make it possible to determine the positions where fatigue cracks are likely to initiate on the as-welded and proof-loaded structures. The equivalent stress fields obtained for both the heterogeneous and homogeneous descriptions are displayed in Fig. 15. For the different loading conditions and material descriptions used in this study, the equivalent stress is maximal at the weld toe, where an important stress concentrations exist. This is consistent with the experimentally observed crack initiation sites (see Fig. 14). These results indicate that, in the present context, the determination of the fatigue crack initiation site does not require considering the microstructural gradients resulting from the welding operation.

The proposed fatigue criterion makes it possible to construct a unique master S–N curve for all of the configurations tested in the present study. The master curve is obtained by plotting the maximum equivalent stress versus the number of cycles to failure. The master

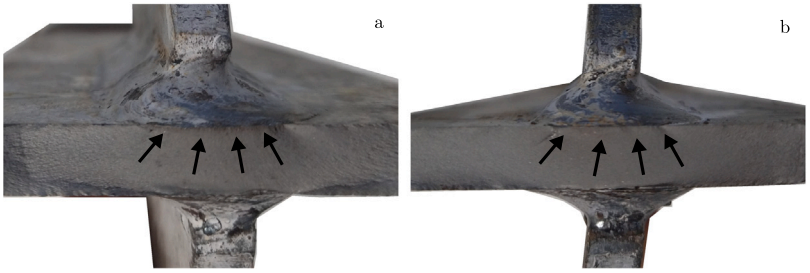

Fig. 14. Fracture surface of (a) an as-welded and (b) a proof-loaded structure, cyclically tested with a load ratio of $R = 0.1$. Multiple crack initiation sites can be observed at the weld toe surface.

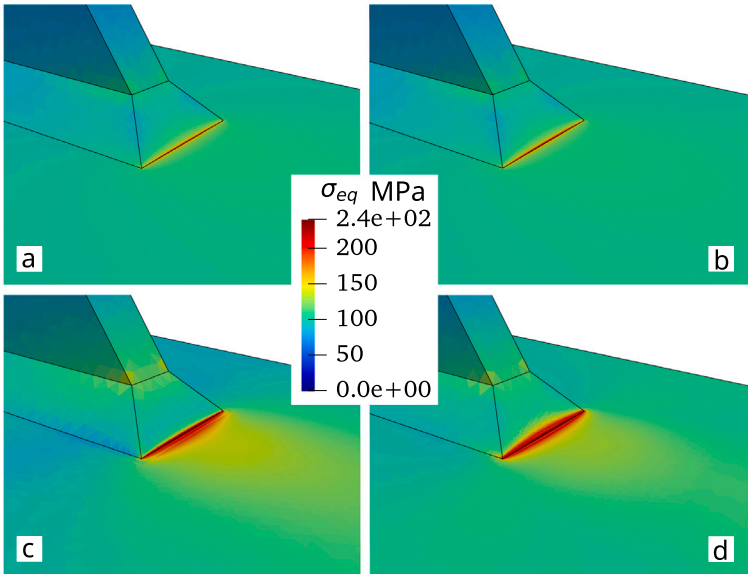

Fig. 15. Equivalent stress distributions in the critical zone obtained for the heterogeneous (a,c) and homogeneous (b,d) descriptions. The results were obtained for as-welded (a,b) and proof-loaded (c,d) specimens with a loading ratio of $R = 0.1$ and a nominal stress range of 169 MPa. An initial nominal stress of 352 MPa was applied to the proof-loaded structure.

curves obtained for the heterogeneous and homogeneous descriptions of the stiffener structures are presented in Figs. 16 and 17, respectively. The Pearson correlation coefficient r^2 is also indicated on each graph. Though the heterogeneous description provides slightly better results, the differences between both descriptions are minor. An accurate description of the elasto-plastic behavior in the vicinity of the weld toe is therefore not essential for the evaluation of the fatigue life.

5.2. Hydrostatic pressure and strain hardening

The numerical model proposed in the present study makes it possible to decouple the effect of the maximum hydrostatic pressure from that of the strain hardening. For this purpose, the S–N curves obtained with the homogeneous description under different assumptions have been constructed with the non-local fatigue criterion. The S–N curve obtained when the role of strain hardening is ignored (i.e. $\phi = 0$) is plotted in Fig. 18. When compared to Fig. 17, the most important discrepancies with the experimental data are observed for specimens loaded in tension–compression ($R = -1$). Alternatively, for stiffener structures loaded with a positive R-ratio ($R = 0.1$), the correspondence with the experimental data is equivalent to that obtained when strain hardening is considered. This result indicate that, for as-welded specimens, the application of a cyclic load is sufficient to promote local plastic deformation at the weld toe, and hence induce strain hardening. For this specific configuration, the additional effect of a proof load on strain hardening remains limited. The S–N curve corresponding to the situation where both the strain hardening effect and the role

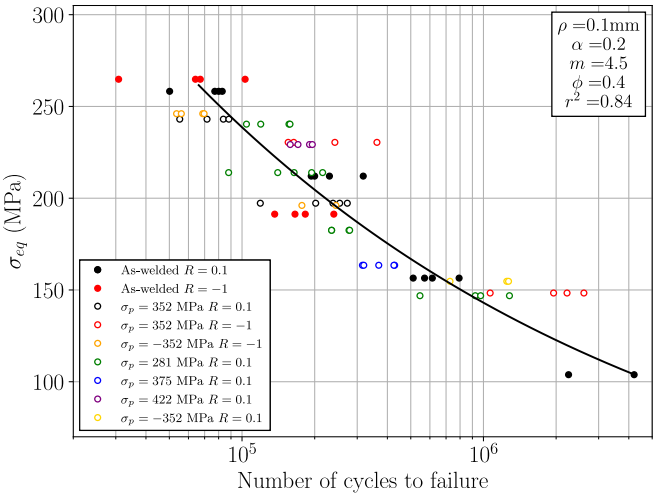

Fig. 16. Numerically determined "master S-N curve" obtained for stiffener structures for different load ratios for as-welded and proof-loaded specimens. An heterogeneous description is adopted for the FEM simulations. Both the strain hardening effect and the role of the maximum hydrostatic pressure are considered for the application of the fatigue criterion.

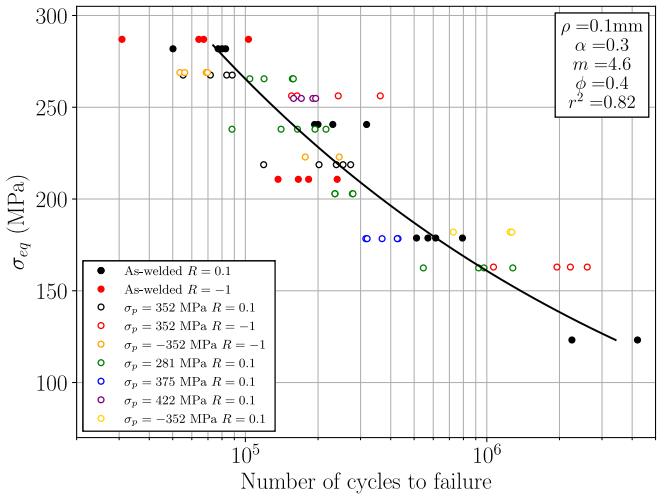

Fig. 17. Numerically determined "master S-N curve" obtained for stiffener structures for different load ratios for the as-welded and proof-loaded specimens. An homogeneous description is adopted for the FEM simulations. Both the strain hardening effect and the role of the maximum hydrostatic pressure are considered for the application of the fatigue criterion.

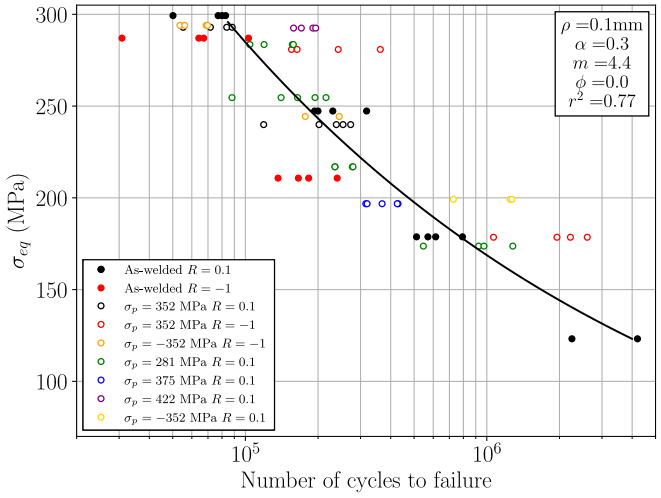

Fig. 18. Numerical S–N curve obtained for stiffener structures for different load ratios for as-welded and proof-loaded specimens. An homogeneous description is adopted for the FEM simulations. The strain hardening effect is ignored but the role of the maximum hydrostatic pressure is considered for the application of the fatigue criterion.

of the maximum hydrostatic pressure are ignored (i.e. $\phi = 0$ and $\alpha = 0$) is displayed in Fig. 19. It is worth mentioning that, in such a situation, only the octahedral shear stress amplitude contributes to the non-local Crossland equivalent stress. The results indicate that this assumption does not provide a consistent description of the impact of a proof load on the fatigue resistance of stiffener structures. Indeed, for many proof-loaded specimens, the fatigue life is largely underestimated by the non-local criterion. The residual hydrostatic pressure resulting from the application of a proof load therefore plays a key role in the improvement of the fatigue resistance.

5.3. Influence of the load ratio

The maximum residual hydrostatic pressures at the fatigue critical location are shown in Fig. 20 for as-welded and proof-loaded (352 MPa) specimens cyclically tested with load ratios of $R = 0.1$ or $R = -1$ and a nominal stress range of 169 MPa. These pressures were calculated at the end of the 60th loading cycle, which corresponds to a steady cyclic behavior. When a proof load under tension is applied

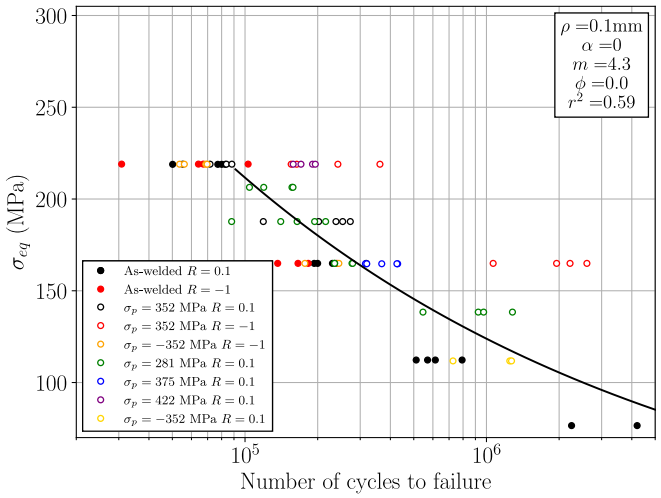

Fig. 19. Numerical S–N curve obtained for stiffener structures for different load ratios for the as-welded and proof-loaded specimens. An homogeneous description is adopted for the FEM simulations. Both the strain hardening effect and the role of the maximum hydrostatic pressure are ignored for the application of the fatigue criterion.

to the stiffener structure, the residual hydrostatic pressure reduces the maximum hydrostatic pressure at the critical location. As discussed earlier, these negative residual hydrostatic pressures largely contribute to the beneficial effect of a proof load on fatigue resistance. However, the proof-loaded specimens tested with a load ratio $R = 0.1$ displays a greater maximum hydrostatic pressure than the proof-loaded specimen tested with a loading ratio $R = -1$, which explains the impact of the load ratio on the fatigue resistance of proof-loaded structures.

Contrary to the proof-loaded specimens, the load ratio has no significant influence on the fatigue resistance of as-welded specimens (see Section 4.1.1). The maximum hydrostatic pressure of as-welded specimens tested with a load ratio of 0.1 nevertheless is about 100 MPa greater than that of as-welded specimens tested with a load ratio of -1. This is in contradiction with the experimental observations that show no sensitivity to the load ratio for as-welded specimens. However, the present analysis does not consider welding-induced residual stresses. For as-welded specimens tested with a load ratio of -1, the maximum non-local von Mises stress at the crack initiation site is lower than the initial yield stress. For this specific configuration, the deformation process is therefore purely elastic. The initial residual stress field resulting from the welding process are therefore not redistributed. As a first approximation, the residual hydrostatic pressure P_{rs} obtained from XRD analyses on a as-welded structure tested with a loading ratio $R = -1$ can be added to the maximum hydrostatic pressure P_m produced by the cyclic loading. As indicated in Fig. 20, when welding-induced residual stresses are considered, structures tested with load ratios of 0.1 and -1 display similar maximum hydrostatic pressures, which is consistent with experimental observations.

6. Conclusions

In this study, the influence of a proof load, or an initial overload, on the fatigue resistance of welded structures has been investigated. For this purpose, stiffener structures were made from S355 structural steel plates and then fatigue-tested with different load ratios. An initial proof load, under either tension or compression, was applied prior to fatigue testing to some of these structures. In comparison with as-welded specimens, a beneficial effect of a proof load on the fatigue resistance is observed, provided that the nominal proof stress exceeds 250 MPa. When the proof load is applied in compression, no visible effect on the fatigue resistance is detected. Also, while the fatigue behavior of as-welded specimens is not influenced by the load ratio, the

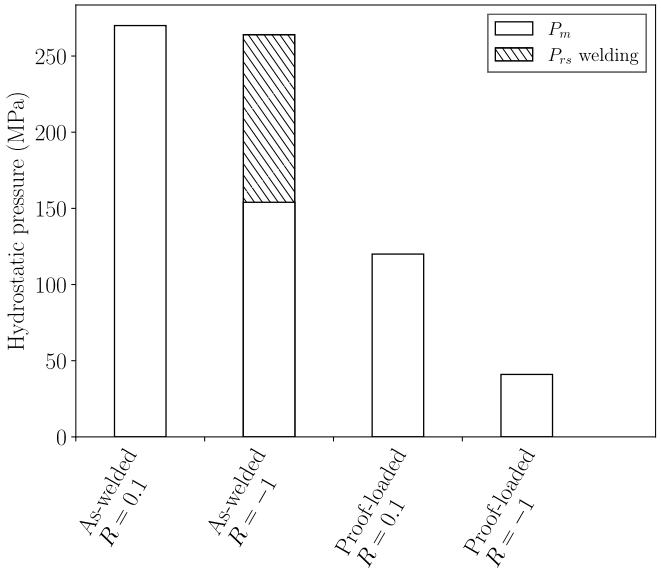

Fig. 20. Maximum hydrostatic pressure of as-welded and proof-loaded structures (352 MPa) tested with a nominal stress range of 169 MPa. For as-welded specimens tested with a loading ratio of −1, the contribution of the residual stress state resulting from welding to the hydrostatic pressure is also indicated (Prs welding). This contribution was evaluated from XRD stress analyses.

fatigue life of proof-loaded specimens decreases when the load ratio is increased from −1 to 0.1. To consider the impact of a proof load on the fatigue resistance, a numerical model has been proposed. The model relies on the elasto-plastic FEM to compute the stress field resulting from a loading history. A non-local fatigue criterion is then used to post-process the stress field and estimate the fatigue life. When compared to the experimental data obtained from XRD analyses, the model correctly reproduces the impact of a proof load on the residual hydrostatic pressure near the weld toe. Also, the non-local fatigue criterion allows clustering of the different fatigue test results on to a single master S–N curve. According to numerical results, although strain hardening participates in improving the fatigue resistance, the beneficial effect of a proof load is mostly attributed to the residual stresses resulting from local plastic deformation near the weld toe. Finally, to consider the impact of a proof load on the fatigue resistance of stiffener structures, the role of mechanical property gradients is negligible.

Declaration of competing interest

The authors declare that they have no known competing financial interests or personal relationships that could have appeared to influence the work reported in this paper.

Acknowledgment

The research is supported by Cetim within the framework of sectorial activities and the Transversal Thematic Project (PTT): Fatigue of welded assemblies.

Appendix

See Table 4.

Table 4
Summary of the fatigue test results.

Proof load (MPa)	Stress amplitude (MPa)	Loading ratio	Number of cycles to failure
0	77	0.1	4 208 852
			2 251 776
0	113	0.1	792 786
			614 123
			570 238
			511 673
0	169	0.1	317 761
			230 186
			199 874
			193 464
0	253	0.1	82 809
			77 128
			50 136
			80 044
281	140	0.1	924 853
			1 281 517
			545 859
			973 410
281	169	0.1	235 072
			234 931
			277 389
			279 119
281	197	0.1	140 569
			194 229
			164 353
			215 713
			88 000
Proof load (MPa)	Stress amplitude (MPa)	Loading ratio	Number of cycles to failure
281	225	0.1	119 533
			104 330
			156 495
			158 014
352	197	0.1	272 951
			201 888
			238 058
			253 802
			119 059
352	253	0.1	71 626
			83 699
			55 208
			88 199
375	169	0.1	428 754
			425 681
			315 368
			319 363
			368 383
422	253	0.1	170 520
			158 319
			190 348
			195 460
−352	113	0.1	1 249 413
			726 858
			1 270 207
Proof load (MPa)	Stress amplitude (MPa)	Loading ratio	Number of cycles to failure
0	169	−1	182 811
			165 734
			240 001
			136 552
0	253	−1	103 006
			64 130
			30 821
			67 176
352	169	−1	2 219 406
			1 952 243
			2 606 671
			1 066 037

(*continued on next page*)

Table 4 (*continued*).

352	253	−1	155 282
			362 113
			242 445
			163 728
−352	169	−1	244 711
			177 022
−352	253	−1	53 566
			68 761
			56 053
			69 659

References

[1] ANSI/ASTM A391-86, proof-testing requirements for special custom design steel chain and attachments.

[2] Masumoto I, Matsuda K, Iwata H, Hasegawa M. Effect of prestrain and hammer peening on fatigue strength improvement of mild steel welded joint. J Japan Weld Soc 1982;51(7):610–6. http://dx.doi.org/10.2207/qjjws1943.51.610.

[3] Hensel J, Nitschke-Pagel T, Dilger K. Effects of residual stresses and compressive mean stresses on the fatigue strength of longitudinal fillet-welded gussets. Weld World 2016;60(2):267–81. http://dx.doi.org/10.1007/s40194-015-0284-6.

[4] Sadeler R, Ozel A, Kaymaz I, Totik Y. The effect of residual stresses induced by prestraining on fatigue life of notched specimens. J Mater Eng Perform 2005;14. http://dx.doi.org/10.1361/10599490523995.

[5] Tsutsumi S, Shibata H, Fincato R, Yonezawa T, Shimanuki H. Effect of pre-overload on fatigue life extension of u-rib steel floor slab root. Q J Japan Weld Soc 2020;38(2):177s–81s.

[6] Schubnell J, Carl E, Farajian M, Gkatzogiannis S, Knödel P, Ummenhofer T, Wimpory R, Eslami H. Residual stress relaxation in hfmi-treated fillet welds after single overload peaks. Weld World 2020;64(6):1107–17. http://dx.doi.org/10.1007/s40194-020-00902-6.

[7] Farajian M, Nitschke-Pagel T, Dilger K. Mechanisms of residual stress relaxation and redistribution in welded high-strength steel specimens under mechanical loading. Weld World 2010;54(11):R366–74. http://dx.doi.org/10.1007/BF03266751.

[8] Schubnell J, Pontner P, Wimpory RC, Farajian M, Schulze V. The influence of work hardening and residual stresses on the fatigue behavior of high frequency mechanical impact treated surface layers. Int J Fatigue 2020;134:105450. http://dx.doi.org/10.1016/j.ijfatigue.2019.105450, URL https://www.sciencedirect.com/science/article/pii/S0142112319305547.

[9] Leitner M, Khurshid M, Barsoum Z. Stability of high frequency mechanical impact (hfmi) post-treatment induced residual stress states under cyclic loading of welded steel joints. Eng Struct 2017;143:589–602. http://dx.doi.org/10.1016/j.engstruct.2017.04.046, URL https://www.sciencedirect.com/science/article/pii/S0141029616312986.

[10] Janardhan G, Dutta K, Mukhopadhyay G. Influence of work hardening on tensile and fatigue behavior of resistance spot-welded dual-phase steel. J Mater Eng Perform 2022. http://dx.doi.org/10.1007/s11665-022-07117-4.

[11] Munier R, Doudard C, Calloch S, Weber B. Towards a faster determination of high cycle fatigue properties taking into account the influence of a plastic pre-strain from selfheating measurements. Procedia Eng 2010;2:1741–50. http://dx.doi.org/10.1016/j.proeng.2010.03.187.

[12] Nishida SI, Zhou C, Hattori N, Wang S. Fatigue strength improvement of notched structural steels with work hardening. Mater Sci Eng: A 2007;468-470:176–83. http://dx.doi.org/10.1016/j.msea.2006.09.120, URL https://www.sciencedirect.com/science/article/pii/S0921509307003139. The McEvily Symposium: Fatigue and Fracture of Traditional and Advanced Materials, TMS 2006.

[13] Fujimura K, Nisitani H, Fukuda T, Fukuda S. Changes in residual stress and successive observations in the fatigue test of workhardened mild steel. WIT Trans Eng Sci 1970;13.

[14] El May M, Saintier N, Palin-Luc T, Devos O. Non-local high cycle fatigue strength criterion for metallic materials with corrosion defects. Fatigue Fract Eng Mater Struct 2015;38:1017–25. http://dx.doi.org/10.1111/ffe.12329.

[15] Bracquart B, Mareau C, Saintier N, Morel F. Experimental study of the impact of geometrical defects on the high cycle fatigue behavior of polycrystalline aluminium with different grain sizes. Int J Fatigue, 31(1): 17–25. 20. http://dx.doi.org/10.1016/j.ijfatigue.2017.12.009.

[16] Heyraud H. Caractérisation expérimentale et modélisation du comportement en fatigue à grand nombre de cycles des structures soudées: application aux engins de manutention (Ph.D. thesis), 2021, URL http://www.theses.fr/2021HESAE029.

[17] Gadouini H, Nadot Y, Rebours C. Influence of mean stress on the multiaxial fatigue behaviour of defective materials. Int J Fatigue 2008;30(9):1623–33. http://dx.doi.org/10.1016/j.ijfatigue.2007.11.010, URL https://www.sciencedirect.com/science/article/pii/S0142112307003222.

[18] Slezak T, Sniezek L. A comparative lcf study of s960ql high strength steel and s355j2 mild steel. Procedia Eng 2015;114:78–85. http://dx.doi.org/10.1016/j.proeng.2015.08.044.

[19] Giraud L. Apports au dimensionnement en fatigue à faible nombre de cycles des assemblages soudés en s355 (Ph.D. thesis), 2020, URL http://www.theses.fr/2020LYSEE002/document.

[20] Frederick CO, Armstrong PJ. A mathematical representation of the multiaxial bauschinger effect. Mater High Temp 2007;24(1):1–26. http://dx.doi.org/10.1179/096034007X207589.

[21] Le V-D, Saintier N, Morel F, Bellett D, Osmond P. Investigation of the effect of porosity on the high cycle fatigue behaviour of cast al-si alloy by x-ray microtomography. Int J Fatigue 2018;106:24–37. http://dx.doi.org/10.1016/j.ijfatigue.2017.09.012.

[22] Heyraud H, Robert C, Mareau C, Bellett D, Morel F, Belhomme B, Dore O. A two-scale finite element model for the fatigue design of large welded structures. Eng Fail Anal 2021;124:105280. http://dx.doi.org/10.1016/j.engfailanal.2021.105280.

[23] Merot P. Effet des défauts de fabrication et de corrosion sur le comportement en fatigue d'un acier 316l obtenu par fabrication additive (Ph.D. thesis), 2021, URL http://www.theses.fr/2021HESAE076/document. Thèse de doctorat dirigée par Morel, Franck et Pessard, Etienne Mécanique-matériaux (AM) Paris, HESAM 2021.

[24] Hobbacher A. Recommandations pour la conception en fatigue des assemblages et des composants soudés. International institute of welding; 2015.

[25] Crossland B. Effect of large hydrostatic pressures on the torsional fatigue strength of an alloy steel. In: Proc. int. conf. on fatigue of metals, Vol. 138. Institution of Mechanical Engineers London; 1956, p. 12.

[26] Sepe R, Greco A, De Luca A, Armentani E, Berto F. Experimental and fem numerical assessment of multiaxial fatigue failure criteria for a rolling stock's seats structure. Eng Fail Anal 2019;102:303–17. http://dx.doi.org/10.1016/j.engfailanal.2019.04.065, URL https://www.sciencedirect.com/science/article/pii/S1350630719302377.

[27] Cristofori A, Livieri P, Tovo R. An application of the implicit gradient method to welded structures under multiaxial fatigue loadings. Int J Fatigue 2009;31(1):12–9. http://dx.doi.org/10.1016/j.ijfatigue.2008.05.007, URL https://www.sciencedirect.com/science/article/pii/S0142112308001400. Fatigue assessment of welded connections.

[28] Radaj D, Sonsino CM, Fricke W. Fatigue assessment of welded joints by local approaches. 2nd ed.. Woodhead Publishing; 2006.

[29] Kaffenberger M, Vormwald M. Considering size effects in the notch stress concept for fatigue assessment of welded joints. Comput Mater Sci 2012;64:71–8. http://dx.doi.org/10.1016/j.commatsci.2012.02.047.

[30] Pedersen M. Thickness effect in fatigue of welded butt joints: A review of experimental works. Int J Steel Struct 2019;19. http://dx.doi.org/10.1007/s13296-019-00254-y.

[31] Xu K, Qiao G, Wang J, Li H, Xiao F. Effect of plastic pre-strain on the fatigue properties of welded joints of x80 lsaw pipes. Int J Fatigue 2020;139:105788. http://dx.doi.org/10.1016/j.ijfatigue.2020.105788.

[32] Okawa T, Shimanuki H, Funatsu Y, Nose T, Sumi Y. Effect of preload and stress ratio on fatigue strength of welded joints improved by ultrasonic impact treatment. Weld World 2013;57(2):235–41. http://dx.doi.org/10.1007/s40194-012-0018-y.

[33] Baumgartner J, Bruder T. Influence of weld geometry and residual stresses on the fatigue strength of longitudinal stiffeners. Weld World 2013;57(6):841–55. http://dx.doi.org/10.1007/s40194-013-0078-7.

[34] Hart PH. Yield strength from hardness data. ARSM, AIM, MWeld; 1975.

[35] Hiraide T, Igi S, Handa T, Tagawa T, Ikeda R, Morita K, Fincato R, Tsutsumi S. Effect of heat affected zone microstructure behavior under cyclic loading on fatigue life of weld joint. Q J Japan Soc 2018;36.

[36] Wang Q, Liu X, Yan Z, Dong Z, Yan D. On the mechanism of residual stresses relaxation in welded joints under cyclic loading. Int J Fatigue 2017;105:43–59. http://dx.doi.org/10.1016/j.ijfatigue.2017.08.016, URL https://www.sciencedirect.com/science/article/pii/S0142112317303432.